This paper appears in IEEE Transactions on Microwave Theory and Techniques, 2024

https://doi.org/10.1109/TMTT.2024.3508767

A Closed-Form Matrix Solution for High-Order Wave Reflection in an Open-Ended Coaxial Line for Rapid Dielectric Spectroscopy

Hossein Asilian Bidgoli[1], Nicola Schieda[2], and Carlos Rossa[1]

***Abstract*—Permittivity spectroscopy using open-ended coaxial probes for material characterization has applications in various fields, including biomedical engineering. The frequency dependent permittivity of a material is extracted from the measured reflection coefficient through a coaxial probe. Current models that relate the reflection coefficient to the dielectric properties of the material struggle to balance accuracy and computational efficiency, limiting their utility in near real-time applications.**

This paper introduces a novel matrix-based closed-form solution of the reflection coefficient of an open-ended coaxial probe. The approach combines full-wave analysis with a Taylor series expansion, leading to a straightforward matrix calculation. By reformulating the forward problem to decouple the material properties from the geometric properties of the probe, the required numerical integral only needs to be calculated once for each probe geometry. This significantly reduces computational time while providing similar or greater accuracy than existing methods. The model has been validated experimentally using two coaxial probes and four reference liquids, achieving an average error of 3.15%. Further validation through 9,600 simulations in Ansys HFSS demonstrated an average error of 2.9%. When applied to inverse problems for estimating material permittivity, the model exhibited an average error of 4.35% while being 376 times faster than existing state-of-the-art models, with similar or enhanced accuracy. These advancements facilitate real-time, full-wave permittivity spectroscopy, offering substantial benefits for medical diagnostics and monitoring.

***Index Terms*—Permittivity spectroscopy; reflection coefficient; closed-form model; open-ended coaxial probe; full-wave model.**

I. Introduction

PERMITTIVITY spectroscopy measures the tendency of a material under test (MUT) to acquire an electric dipole moment when exposed to an alternating electromagnetic field. The frequency-dependent complex permittivity of the MUT is often used to characterise and monitor different materials in diverse domains encompassing biology [1]–[3], electronics [4], [5], agriculture [6], [7], civil engineering [8], [9] and more. In biomedical engineering, permittivity spectroscopy may be used for cancer detection since the permittivity of cancerous tissues differ significantly from their healthy counterparts in a frequency ranging from 0.5 GHz to 10 GHz [10]–[18]. In general, cancerous tissues have higher water content than healthy tissues, which increases its permittivity [19]–[21].

The method of choice for permittivity spectroscopy of biological tissue uses open-ended coaxial probes [3], [22]. To estimate the permittivity of the MUT, an electromagnetic wave is directed through the probe toward the aperture in contact with the MUT. Upon reaching the material, some of the wave is reflected back to the source. The magnitude and phase of the reflected wave are directly tied to the material's complex permittivity. The ratio of the amplitude of reflected wave to the incident wave is known as the reflection coefficient, from which the permittivity is calculated. However, developing an accurate model which links the permittivity of the MUT to the reflection coefficient is a complex task. Current methods suffer from a trade-off between accuracy and computational costs.

Admittance models were the first to correlate the measured reflection coefficient (R_0) with the material's permittivity by taking into account the propagation of electromagnetic waves inside the probe and their interaction with the material [23]. To improve computational efficiency, these models were later refined using Taylor series expansions [24], [25]. However, admittance models are not accurate, especially at higher frequencies, were the effect of higher wave modes neglected in the model becomes more prominent. In response, full-wave models have been developed to incorporate these higher-order modes [26], [27], but they are time-consuming, requiring repeated numerical evaluation of integrals subjected to singularities for every measurement. A model that can simultaneously achieve both high accuracy and computational efficiency would enable real-time applications of permittivity spectroscopy, potentially making it a standard diagnostic and monitoring modality in healthcare.

In this paper, we introduce a novel physics-based model of the reflection coefficient of an open-ended coaxial probe using full-wave analysis that works in real-time. To the best of our knowledge, this is the first *closed-form and full-wave* solution in the literature that provides the reflection coefficient given the MUT permittivity. Some preliminary results related to this work were presented in [28]. To clearly position our contribution with respect to the state-of-the-art, in Section II we begin with an in-depth mathematical review to describe the electromagnetic field inside the probe and MUT, and the most comprehensive models of the reflection coefficient that were introduced in the literature in the last five decades and discuss their limitations. We then introduce in Section III our

[1]H. Asilian and C. Rossa are with the Department of Systems and Computer Engineering, Carleton University, Ottawa, ON, Canada

[2]N. Schieda is with the Department of Radiology, Radiation Oncology and Medical Physics, University of Ottawa, Ottawa, ON, Canada

This research is supported by the Cancer Research Society and the Canadian Institutes of Health Research (grant #944486).

Cette recherche est appuyée par la Société de recherche sur le cancer et les Instituts de recherche en santé du Canada (subvention no 944486).

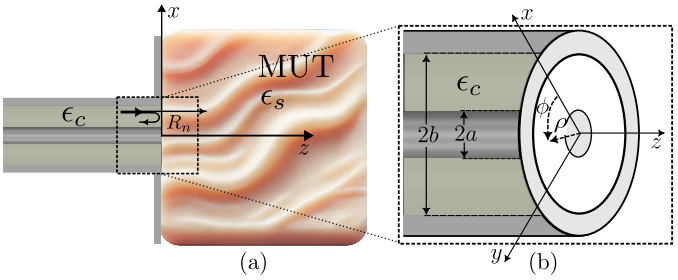

Fig. 1. (a) Open-ended coaxial probe in contact with a MUT of permittivity ϵ_s. The magnitude of the reflected wave depends on the reflection coefficient R_n. (b) The coaxial probe aperture with cylindrical coordinates ρ and ϕ expressed in the reference frame xyz located at the centre of the aperture. a and b are the inner and outer radii of the probe, and ϵ_c is the relative permittivity of the dielectric inside the probe, which fills the space between the inner and outer conductors.

proposed new model. It combines a full-wave analysis with a Taylor series expansion that reduces the forward problem to a simple matrix inversion. Our model addresses a crucial gap in the literature and is expected to:

1) Solve well-known inaccuracies and limitations of single mode models by considering higher order modes,
2) Improve the accuracy over full-wave methods in certain scenarios by reducing the dependency on numerical calculation of infinite integrals, and
3) Significantly reduce the computational time required in full-wave analysis.

While current fast single-mode models lack accuracy, and accurate full-wave models are time-consuming, our model achieves both accuracy and efficiency simultaneously. Its efficiency becomes particularly evident, and even more advantageous compared to other full-wave methods when the model is applied to an inverse problem to extract the medium's permittivity. The fast and accurate model is accomplished by decoupling the material parameters from time-consuming numerical integrals with singularities, and later reducing the forward problem to a straightforward matrix calculation.

The model's performance is evaluated experimentally using two different coaxial probes immersed in methanol, acetone, 1-propanol, and dimethyl sulfoxide (DMSO) in a frequency range of 1 GHz to 10 GHz. The model's accuracy is further assessed through 9,600 simulations in Ansys HFSS to cover a broader range of MUT permittivities. The experimental and simulation results show an average error in estimating the reflection coefficient of 3.15% and 2.9%, respectively. Finally, the model is used in an inverse problem to determine the permittivity of the MUT. The results reveal an average error of 4.35% while providing computational speeds 376 times faster than existing state-of-the-art full-wave models. This model is a crucial first step towards full-wave, real-time permittivity spectroscopy, which has many applications in medicine.

II. Literature Review

Fig. 1 illustrates a coaxial probe opening to a MUT. The objective is to determine the complex permittivity ϵ_s of the MUT from the phase and magnitude of the reflected electromagnetic wave, which is measured at other end of the probe by a vector network analyzer (VNA). The permittivity is therefore estimated indirectly, meaning that an accurate model linking the reflection coefficient to the permittivity of the MUT is required. In this section, we review the most comprehensive models available in the literature.

The process begins by transmitting an transverse electromagnetic (TEM) wave along the coaxial probe toward the MUT. The TEM wave has an electric and a magnetic field perpendicular to the direction of propagation and has no field component parallel to the direction of propagation. Upon reaching the impedance discontinuity at the aperture, part of the wave travels further into the MUT and the rest reflects back to the source through the probe. Along with the reflected TEM wave, higher-order modes created at the aperture also reflect back. These higher-order modes have distinct field patterns and are all evanescent (they decay rapidly as they propagate in the line). Only the TEM wave travels back to the source of the coaxial probe. The reflection coefficient, hereafter denoted by R_0, can now be formally defined as the ratio of the amplitude of the primary mode of the reflected TEM wave to the transmitted TEM. Thus, to form a model to extract the permittivity of the MUT, all higher-order modes and radiated waves must be considered. In the next subsections, the equations governing the electric and magnetic fields inside the coaxial probe and radiated from the aperture are presented.

A. Electric and Magnetic Fields Inside the Coaxial Probe

Consider the coaxial transmission line with an outer radius of b and an inner conductor radius of a from Figure 1. A reference frame with axes x and y is placed at the centre of the aperture with the z axis parallel to the line and such that the line terminates and makes contact with the MUT at $z = 0$. The incident TEM has an electric field in the radial direction (E_ρ) and magnetic filed in the angular direction (H_ϕ).

Higher-order modes inside a coaxial cable (also known as waveguide modes) are transverse electric TE_{mn} and transverse magnetic TM_{mn}, each having an extra magnetic and electric field component, respectively, parallel to the direction of propagation compared to the TEM wave [29], [30]. TEM mode is solution to the Laplacian wave equation, while the TE_{mn} and TM_{mn} modes are solutions to the Helmholtz wave equations. In the coaxial line, the excitation occurs via a TEM wave, which lacks angular variation (ϕ in Fig. 1(b)). Consequently, only higher-order modes with no angular dependence can be excited, specifically the TM_{0n} modes.

The radial electric field E_ρ can be expressed as:

$$E_\rho(\rho, z) = A_0 \left[f_0(\rho) \mathrm{e}^{-\gamma_0 z} + \sum_{n=0}^{\infty} R_n f_n(\rho) \mathrm{e}^{\gamma_n z} \right] \quad (1)$$

The temporal dependency is dropped for simplicity. In the expression above, A_0 is the amplitude of the primary mode of the electric field, ρ is the radial distance in cylindrical coordinate (see Fig. 1), $f_n(\rho)$ and γ_n are the radial functions and the propagation factor of mode n, respectively, and R_n is the reflection coefficient of each mode. Of particular interest is the primary mode reflection coefficient R_0 (for $n = 0$), which is the only measurable parameter by the VNA.

The azimuthal magnetic field H_ϕ is

$$H_\phi(\rho,z) = j\omega\epsilon_0\epsilon_c A_0 \left[\frac{f_0(\rho)}{\gamma_0} \mathrm{e}^{-\gamma_0 z} - \sum_{n=0}^{\infty} R_n \frac{f_n(\rho)}{\gamma_n} \mathrm{e}^{\gamma_n z} \right], \tag{2}$$

in which ϕ is the azimuth angle of the aperture (as in Fig. 1), ϵ_0 is the vacuum permittivity, ϵ_c is the constant, frequency-independent relative permittivity of the dielectric inside the probe, and ω is the radial frequency.

The radial function of the primary mode ($n = 0$) is:

$$f_0(\rho) = \frac{N_0}{\rho} \tag{3}$$

where the normalization factor N_0 is:

$$N_0 = 1/\sqrt{\ln(b/a)} \tag{4}$$

The primary mode propagation factor is:

$$\gamma_0 = j\sqrt{\epsilon_c}(\omega/c_0) \tag{5}$$

where c_0 is the speed of light in vacuum. The radial functions $f_n(\rho)$ of the higher orders are:

$$f_n(\rho) = N_n \left[J_1(p_n\rho)\, Y_0(p_n a) - Y_1(p_n\rho)\, J_0(p_n a) \right], \tag{6}$$

where J_m and Y_m refer to the m^{th} order Bessel functions of the first and second kinds, respectively. The eigenvalues, denoted as p_n, are the solutions to

$$Y_0(p_n a)J_0(p_n b) = J_0(p_n a)Y_0(p_n b) \quad n > 0. \tag{7}$$

In (6), the normalization factor N_n of higher order modes is

$$N_n = \frac{\pi p_n}{\sqrt{2}} \left[\frac{J_0^2(p_n a)}{J_0^2(p_n b)} - 1 \right]^{1/2} \qquad n > 0 \tag{8}$$

And the higher order propagation factor γ_n in (1) and (2) can be defined as:

$$\gamma_n = \sqrt{p_n^2 - \epsilon_c(\omega/c_0)^2} \quad n > 0 \tag{9}$$

Equations (1) and (2) describe the transmitted and reflected waves within the coaxial cable, which also radiate through the aperture towards the MUT. While both electric and magnetic fields exist inside the MUT, the reflection coefficient model requires only one of these fields. The next subsection details the formulation of the radiated magnetic field.

B. Radiated Magnetic Field from the Aperture

The open-end of the coaxial probe radiates into the MUT on the positive side of the z-axis, as in Fig. 1. The radiated magnetic filed can be related to the tangential electric field $E_\rho(\rho',\phi')$ at $z = 0$ using Huygens' principle and image theory. Here, prime denotes the coordinates of the source point. The detailed analysis of the radiated magnetic field resulting from the aperture fields is extensively discussed in [29]. Since there is no geometry variation in the ϕ' direction, it follows that $E_\rho(\rho',\phi') = E_\rho(\rho')$.

Given every point on the aperture as a source point, the total magnetic field is the integral of all these source points, that is, from $\rho = a$ to $\rho = b$ and $\phi = 0$ to $\phi = 2\pi$, and given as:

$$H_\phi(\rho,z) = \frac{jk_s^2}{2\pi\omega\mu_0} \int_a^b \int_0^{2\pi} E_\rho(\rho') \frac{e^{-jk_s r}}{r} \cos\psi \rho' \mathrm{d}\psi \mathrm{d}\rho' \tag{10}$$

where $\psi = \phi - \phi'$ and $r = \sqrt{\rho^2 - \rho^2 - 2\rho\rho' \cos\psi + z^2}$. Finally, the MUT wave number k_s is a function of its complex permittivity ϵ_s:

$$k_s = \omega\sqrt{\mu_0\epsilon_0\epsilon_s}, \tag{11}$$

and the MUT complex relative permittivity is:

$$\epsilon_s = \epsilon' - j\epsilon'', \tag{12}$$

where ϵ' and ϵ'' are the real and imaginary part of relative permittivity of the MUT, respectively. All three parameters, ϵ_s, ϵ', and ϵ'' are frequency-dependent; however, for simplicity, the explicit notation for frequency is dropped. The waves inside the coaxial probe and the wave radiated to the MUT from the aperture can be related by the boundary condition as is discussed in the following subsection.

C. Boundary Condition Across the Aperture

The boundary conditions must ensure that the tangential magnetic field of the aperture inside and outside the probe are continuous. This condition is satisfied by equating (2) and (10) at $z = 0$:

$$\begin{aligned} &j\omega\epsilon_0\epsilon_c A_0 \left[\frac{f_0(\rho)}{\gamma_0} - \sum_{n=0}^{\infty} R_n \frac{f_n(\rho)}{\gamma_n} \right] = \\ &\frac{jk_s^2}{2\pi\omega\mu_0} \int_a^b \int_0^{2\pi} E_\rho(\rho') \frac{e^{-jkr}}{r} \cos\psi \rho' \mathrm{d}\psi \mathrm{d}\rho' \end{aligned} \tag{13}$$

In some methods the Somerfeld identity is used to convert $\frac{e^{-jk_s r}}{r}$ to be expressed in terms of Bessel functions, then (13) can be rewritten as:

$$\begin{aligned} &j\omega\epsilon_0\epsilon_c A_0 \left[\frac{f_0(\rho)}{\gamma_0} - \sum_{n=0}^{\infty} R_n \frac{f_n(\rho)}{\gamma_n} \right] = \\ &\frac{jk_s^2}{\omega\mu_0} \int_0^{\infty} \int_a^b E_\rho(\rho') \frac{J_1(\zeta\rho) J_1(\zeta\rho')\, \zeta}{(\zeta^2 - k^2)^{1/2}} \rho' \mathrm{d}\rho' \mathrm{d}\zeta \end{aligned} \tag{14}$$

In the following subsections, various proposed models in the literature that use the aforementioned equations to determine R_0 based on the permittivity of the MUT are presented.

Having established the mathematical foundation of the EM wave inside the probe, we can now review the three most common models that attempt to relate it to the MUT properties.

D. Single-Mode, Admittance and Closed-Form Models

The simplest model, first presented in [23], relates the normalized admittance y_s of the coaxial probe exposed to the MUT and its reflection coefficient as:

$$y_s = \frac{1 - R_0}{1 + R_0} \tag{15}$$

A common approach for calculating the normalized admittance of the coaxial probe is to replace the electric field in the right

side of (14) with its TEM mode, i.e., $E(\rho) = A_0 f_0(\rho)$ [25], [31]. Then, by multiplying both sides of the resulting equation by $f_0(\rho)\rho$ and integrating them from a to b over ρ, gives:

$$j\omega\epsilon_0\epsilon_c A_0 \left[\int_a^b \frac{f_0(\rho)^2}{\gamma_0}\rho \mathrm{d}\rho - \sum_{n=0}^{\infty} R_n \int_a^b \frac{f_0(\rho) f_n(\rho)}{\gamma_n}\rho \mathrm{d}\rho\right] = \frac{jk_s^2}{\omega\mu_0}\int_0^{\infty}\int_a^b\int_a^b A_0 f_0(\rho) f_0(\rho') \frac{J_1(\zeta\rho)J_1(\zeta\rho')\,\zeta}{(\zeta^2-k^2)^{1/2}}\rho\rho' \mathrm{d}\rho'\mathrm{d}\rho\mathrm{d}\zeta \tag{16}$$

All of the higher order TM_{0n} modes are eliminated as their integral is zero due orthogonality of radial functions. The final term for the normalized admittance after a few steps is:

$$y_s = \frac{1-R_0}{1+R_0} = \frac{jk_s}{(\epsilon_i/\epsilon_0)^{1/2}\ln(b/a)}\int_0^{\infty}\frac{\mathrm{d}\zeta}{\zeta\,(\zeta^2-k_s^2)^{1/2}} \cdot \left[J_0(\zeta a) - J_0(\zeta b)\right]^2. \tag{17}$$

The infinite integral above must be solved numerically since it has no analytical solution. While this method is simpler compared to the full-wave method (presented in the next subjection), it compromises accuracy by disregarding higher-order modes. Additionally, the numerical integration makes it computationally intensive. However, a closed-form model can be achieved by multiplying both sides of (13) by $f_0(\rho)\rho$ and replacing the exponential function $e^{-jk_s r}$ with a Taylor expansion. By integrating both sides from a to b over ρ, and after some simple manipulators, we obtain:

$$y_s = \frac{k_s^2}{2\pi k_c \ln(b/a)}\left\{\left[I_1 - \frac{k_s^2 I_3}{2} + \frac{k_s^4 I_5}{24} - \frac{k_s^6 I_7}{720} + \cdots\right] + j\left[I_2 k_s - \frac{k_s^3 I_4}{6} + \frac{k_s^5 I_6}{120} - \cdots\right]\right\} \tag{18}$$

where

$$I_n = \int_a^b\int_a^b\int_0^{2\pi} r^{n-2}\cos\psi \mathrm{d}\psi\mathrm{d}\rho\mathrm{d}\rho' \quad n = 1, 2, 3\cdots \tag{19}$$

In this expansion, the I_n terms are independent of the material and rely solely on the properties of the probe [3], [32]. Therefore, these coefficients only need to be calculated once, unlike the previous formulation that requires the calculation of the integral for every measurement frequency.

Although this model is simple, it fails when the aperture diameter is close to the operating frequency wavelength. To address this limitation, the coefficients of the Taylor expansion may be optimized through analytical calculations [33] or by model fitting, like we did in [3]. However, modeling errors still remain since higher modes are neglected. Considering all of the propagating modes inside the coaxial probe when replacing $E_\rho(\rho')$ in (13) or in (14) will lead to better modelling accuracy. This is presented next.

E. Full-Wave Orthogonal Model

To consider all wave modes, it is sufficient to replace the electric field $E_\rho(\rho')$ in (14) with its full-wave form (1). Thus, (14) can be rewritten as [26], [34]:

$$j\omega\epsilon_0\epsilon_c\left[\frac{f_0(\rho)}{\gamma_0} - \sum_{n=0}^{\infty} R_n\frac{f_n(\rho)}{\gamma_n}\right] = j\omega\epsilon_0\epsilon_s\int_0^{\infty}\int_a^b \left[f_0(\rho') + \sum_{n=0}^{\infty} R_n f_n(\rho')\right]\frac{J_1(\zeta\rho)J_1(\zeta\rho')\,\zeta}{(\zeta^2-k^2)^{1/2}}\rho'\mathrm{d}\rho'\mathrm{d}\zeta \tag{20}$$

Cancelling out A_0 from both sides of the original equation. This manipulation gives raise to an infinite number of unknown reflection coefficients R_n, one for each considered mode (recall that the previous models only had one unknown parameter, i.e., R_0). To solve for the unknown R_n we need a system of equations, which is usually derived from (21). One method is to leverage the orthogonality property of the radial functions $f_n(\rho)$. Then, each equation in this system of equations is obtained by multiplying both sides of (20) by $f_m(\rho)\rho$, and integrating them from a to b over ρ:

$$\epsilon_c\int_a^b f_m(\rho)\left[\frac{f_0(\rho)}{\gamma_0} - \sum_{n=0}^{\infty} R_n\frac{f_n(\rho)}{\gamma_n}\right]\rho\mathrm{d}\rho = \epsilon_s\int_0^{\infty}\int_a^b\int_a^b \left[f_0(\rho') + \sum_{n=0}^{\infty} R_n f_n(\rho')\right]\frac{J_1(\zeta\rho)J_1(\zeta\rho')\,\zeta}{(\zeta^2-k^2)^{1/2}}\rho\rho'\mathrm{d}\rho'\mathrm{d}\rho\mathrm{d}\zeta \tag{21}$$

By substituting the analytical solutions of the integrals over both ρ and ρ' results in:

$$\epsilon_c\int_a^b f_m(\rho)\left[\frac{f_0(\rho)}{\gamma_0} - \sum_{n=0}^{\infty} R_n\frac{f_n(\rho)}{\gamma_n}\right]\rho\mathrm{d}\rho = \epsilon_s\int_0^{\infty} D_m(\zeta)\left[D_0(\zeta) + \sum_{n=0}^{\infty} R_n D_n(\zeta)\right]\frac{\zeta}{(\zeta^2-k^2)^{1/2}}\mathrm{d}\zeta \tag{22}$$

where $D_n(\zeta)$ is:

$$\begin{aligned} D_0(\zeta) &= \frac{1}{\sqrt{\ln(b/a)}}\frac{1}{\zeta}\left[J_0(\zeta a) - J_0(\zeta b)\right] && n = 0 \\ D_n(\zeta) &= \frac{2}{\pi}\frac{N_n}{p_n}\frac{1}{J_0(p_n b)}\frac{\zeta}{p_n^2-\zeta^2}\cdot \\ &\quad \left[J_0(\zeta b)J_0(p_n a) - J_0(\zeta a)J_0(p_n b)\right] && n > 0 \end{aligned} \tag{23}$$

A more comprehensible representation of (22) is, for $m = 0$:

$$\sum_{n=0}^{\infty} R_n\mathcal{B}_{0n} + R_0\frac{\epsilon_c\alpha_0}{\epsilon_s\gamma_0} = \frac{\epsilon_c\alpha_0}{\epsilon_s\gamma_0} - \mathcal{B}_{00} \tag{24}$$

and for $m > 0$:

$$\sum_{n=0}^{\infty} R_n\mathcal{B}_{mn} + R_m\frac{\epsilon_c\alpha_m}{\epsilon_s\gamma_m} = -\mathcal{B}_{m0}. \tag{25}$$

For α_m we have:

$$\alpha_m = \int_a^b f_m(\rho)^2\rho\mathrm{d}\rho \tag{26}$$

with

$$\mathcal{B}_{mn} = \int_0^{\infty}\frac{D_m(\zeta)D_n(\zeta)\zeta}{(\zeta^2-k_s^2)^{1/2}}\mathrm{d}\zeta. \tag{27}$$

While this model provides better accuracy than single mode models, it is more time-consuming as it involves $N\times(N+1)$

numerical integrals for each measurement frequency. A simpler way to construct the system of equations from (20) is to use the point-matching method, which require N fewer integrals.

F. Full-Wave Point-Matching Model

The point-matching method builds the system of equations by equalizing the two sides of (20) over a number of points having the same radii at the aperture ρ. As per [26] for fast convergence these points can be determined based on the mean of the internal and external distributions of matching points, that is:

$$\rho_m = a + \frac{b-a}{2}\left[\frac{i-1}{N-1} + \frac{2i-1}{2N}\right], \quad i = 1, 2, \cdots, N. \tag{28}$$

By replacing ρ with ρ_m in (20), and rearranging the incident wave terms on the right side of the equation and the reflected waves terms on the left side, we get:

$$\sum_{n=0}^{\infty} R_n \left[\frac{f_n(\rho_m)}{\gamma_n} + \frac{\epsilon_s}{\epsilon_c}\int_a^b f_n(\rho')\rho' \mathrm{d}\rho' \int_0^{\infty} \frac{J_1(\zeta\rho_m)J_1(\zeta\rho')\zeta \mathrm{d}\zeta}{(\zeta^2 - k^2)^{1/2}}\right] = \frac{f_0(\rho_m)}{\gamma_0} - \frac{\epsilon_s}{\epsilon_c}\int_a^b f_0(\rho')\rho' \mathrm{d}\rho' \int_0^{\infty} \frac{J_1(\zeta\rho_m)J_1(\zeta\rho')\zeta \mathrm{d}\zeta}{(\zeta^2 - k^2)^{1/2}} \tag{29}$$

Dividing this equation by its right-hand side yields:

$$\sum_{n=0}^{\infty} R_n W_{nm} = 1, \tag{30}$$

in which

$$W_{nm} = \frac{f_n(\rho_m)/\gamma_n + (\epsilon_s/\epsilon_c)\, I_n(\rho_m)}{f_0(\rho_m)/\gamma_0 - (\epsilon_s/\epsilon_c)\, I_0(\rho_m)} \tag{31}$$

and

$$I_n(\rho_m) = \int_0^{\infty} \frac{J_1(\zeta\rho_m)\zeta}{\sqrt{\zeta^2 - k_1^2}} \cdot \int_a^b f_n(\rho')\, J_1(\zeta\rho')\rho' d\rho' d\zeta\,. \tag{32}$$

By integrating over ρ', we have:

$$I_n(\rho_m) = \int_0^{\infty} \frac{J_1(\zeta\rho_m)\zeta}{\sqrt{\zeta^2 - k_1^2}} D_n(\zeta)\, d\zeta \tag{33}$$

Although this method is simpler than the previous methods, the integrals for calculating $I_n(\rho_m)$s are subjected to singularities, and they must be computed for every frequency, which is computationally expensive. Even more time consuming is the process of determining the permittivity of the MUT through a resulting iterative inverse problem over the forward model, making real-time measurements virtually impossible [35]. Clearly, none of the presented models provide a suitable balance between accuracy and computational time. Our newly proposed model bridges this evident gap in the literature by overcoming limitations. Our model is introduced next.

III. Proposed Full-Wave, Closed-Form Model

To circumvent the numerical integration in the reflection coefficient equations, we note that the only term in (21) that depends on the MUT properties is $e^{-jk_s r}$ on the right hand side of the equation. The remaining terms are either the known TEM or TM wave modes, or depend only on the geometry and permittivity of the probe. To solve for R_n in (21), instead of using Sommerfeld identity, we begin by replacing the exponential term with a corresponding Taylor series expansion, similarly to what has been proposed for TEM-only models [18], [25], [32]:

$$\frac{e^{-jkr}}{r} = \sum_{p=0}^{\infty} \frac{(-jk_s)^p r^{p-1}}{p!} \tag{34}$$

This manipulation will lead to several integrals that are solely a function of the probe geometry, therefore the MUT properties (k_s) can then be taken out of these integrals. It follows that after the expansion (21) changes to

$$j\omega\epsilon_0\epsilon_c \left[\frac{f_0(\rho)}{\gamma_0} - \sum_{n=0}^{\infty} R_n \frac{f_n(\rho)}{\gamma_n}\right] = \frac{jk_s^2}{2\pi\omega\mu_0}\int_a^b \int_0^{2\pi} \left[f_0(\rho') + \sum_{n=0}^{\infty} R_n f_n(\rho')\right]\left[\sum_{p=0}^{\infty} \frac{(-jk_s)^p r^{p-1}}{p!}\right] \cos\psi \rho' \mathrm{d}\psi \mathrm{d}\rho' \tag{35}$$

Both sides of the equality in (35) are functions of ρ. To establish a system of equations to solve for R_n and eliminate the dependency on ρ, we multiply both sides of (35) by $f_m(\rho)\rho$ and integrate over ρ from a to b:

$$j\omega\epsilon_0\epsilon_c \int_a^b \left[\frac{f_m(\rho)f_0(\rho)}{\gamma_0} - \sum_{n=0}^{\infty} R_n \frac{f_m(\rho)f_n(\rho)}{\gamma_n}\right] \mathrm{d}\rho = \frac{jk_s^2}{2\pi\omega\mu_0}\int_a^b \int_a^b \int_0^{2\pi} \left[f_m(\rho)f_0(\rho') + \sum_{n=0}^{\infty} R_n f_m(\rho) f_n(\rho')\right] \left[\sum_{p=0}^{\infty} \frac{(-jk_s)^p r^{p-1}}{p!}\right] \cos\psi\rho' \mathrm{d}\psi \mathrm{d}\rho' \mathrm{d}\rho \tag{36}$$

In (36) the orthogonality of Bessel function, i.e.,

$$\int_a^b f_n(\rho) f_m(\rho) \rho \mathrm{d}\rho = 0 \quad \textit{if} \quad n \neq m, \tag{37}$$

entails that only one integral on the left side of (36) is non-zero. Thus, for $m = 0$, (36) we obtain:

$$\frac{\epsilon_c}{\epsilon_s\gamma_0}(1 - R_0)\int_a^b f_0^2(\rho)\rho\, \mathrm{d}\rho = \frac{1}{2\pi}\int_a^b \int_a^b \int_0^{2\pi} \left[(1 + R_0) f_0(\rho') + \sum_{n=1}^{\infty} R_n f_n(\rho')\right] \left[\sum_{p=0}^{\infty} \frac{(-jk_s)^p r^{p-1}}{p!}\right] f_0(\rho) \cos\psi \rho' \mathrm{d}\psi\, \mathrm{d}\rho'\, \mathrm{d}\rho \tag{38}$$

And for $m > 0$, we have:

$$\frac{\epsilon_c}{\epsilon_s \gamma_m}(-R_m)\int_a^b f_0^2(\rho)\rho\,\mathrm{d}\rho = \frac{1}{2\pi}\int_a^b\int_a^b\int_0^{2\pi}\left[(1+R_0)f_0(\rho') + \sum_{n=1}^{\infty} R_n f_n(\rho')\right] \left[\sum_{p=0}^{\infty}\frac{(-jk_s)^p r^{p-1}}{p!}\right] f_m(\rho)\cos\psi\rho\rho'\mathrm{d}\psi\,\mathrm{d}\rho'\,\mathrm{d}\rho \tag{39}$$

After applying the Taylor series expansion to these equations, k_s can be pulled out of the integrals, leaving only the α_m integrals on the left side of (38) and (39), and β_{mnp} on the right side of these equations. Then, α_m is:

$$\alpha_m = \int_a^b f_m^2(\rho)\rho\mathrm{d}\rho \tag{40}$$

And for β_{mnp}:

$$\beta_{mnp} = \frac{1}{2\pi}\int_a^b\int_a^b\int_0^{2\pi}\frac{r^{p-1}}{p!}f_n(\rho')f_m(\rho)\rho'\rho\cos\psi\mathrm{d}\psi\mathrm{d}\rho'\mathrm{d}\rho \tag{41}$$

Replacing the integrals with these terms, (38) and (39) may be rewritten as a double summations, i.e.,

$$(1-R_0)\frac{\epsilon_c}{\epsilon_s\gamma_0}\alpha_0 = (1+R_0)\sum_{p=0}^{\infty}(-jk_s)^p\beta_{00p} + \sum_{n=1}^{\infty}R_n\sum_{p=0}^{\infty}(-jk_s)^p\beta_{0np} \tag{42}$$

And for $m > 0$:

$$(-R_m)\frac{\epsilon_c}{\epsilon_s\gamma_m}\alpha_m = (1+R_0)\sum_{p=0}^{\infty}(-jk_s)^p\beta_{m0p} + \sum_{n=1}^{\infty}R_n\sum_{p=0}^{\infty}(-jk_s)^p\beta_{mnp} \tag{43}$$

Now, let us rearrange these equations with the reflection coefficients term on the left side, and the constant values are on the right side of the equation:

$$\sum_{n=0}^{\infty}R_n\sum_{p=0}^{\infty}(-jk_s)^p\beta_{0np} + R_0\frac{\epsilon_c\alpha_0}{\epsilon_s\gamma_0} = \frac{\epsilon_c\alpha_0}{\epsilon_s\gamma_0} - \sum_{p=0}^{\infty}(-jk_s)^p\beta_{00p} \tag{44}$$

$$\sum_{n=0}^{\infty}R_n\sum_{p=0}^{\infty}(-jk_s)^p\beta_{mnp} + R_m\frac{\epsilon_c\alpha_m}{\epsilon_s\gamma_m} = -\sum_{p=0}^{\infty}(-jk_s)^p\beta_{m0p} \tag{45}$$

Finally, these equations can be expressed as a simple matrix multiplication:

$$AR = B \tag{46}$$

where A and B are given in (17) and (18). In these matrices the sums are defined from $p = 0$ to $p \to \infty$, i.e., $\sum_{p=0}^{\infty} \to \sum$. These limits are omitted for simplicity. Finally, R_0 is simply found as the first cell of the vector $R = (A^{-1})B$.

Unlike the previously reported models, all coefficients in A must be calculated only once for each probe, as they are independent from the MUT properties. Our newly proposed model simplifies to a simple matrix operation, which is inherently much faster, especially with modern CPUs and GPUs optimized for vector calculation.

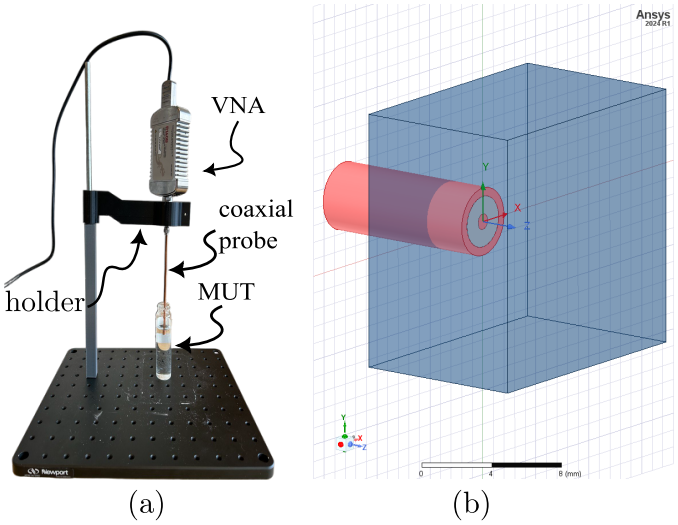

Fig. 2. (a) Measurement setup used for model validation with a coaxial probe placed in the MUT and connected to vector network analyzer. (b) Full-wave simulation of the same open-ended coaxial probe (red) inside the MUT (blue cube) in Ansys.

IV. Model Validation

In this section, the proposed reflection coefficient model is validated experimentally and through simulations. Then, we employ the model in a inverse problem to estimate the MUT permittivity. Modelling error and processing time are then evaluated and compared against the single-mode closed-form model, and the full-wave point-matching model.

We consider two standard 50 Ω coaxial cables, hereafter referred to as the thick and slim probes. The thick probe has a relative permittivity of $\epsilon_c = 2.08$ with inner and outer radii of $a = 0.46$ mm and $b = 1.5$ mm, respectively. The slim probe has a relative permittivity of $\epsilon_c = 1.8$ with inner and outer radii of $a = 0.14$ mm and $b = 0.43$ mm, respectively. The number of modes and the degree of the Taylor expansion are set to $M = N = 5$ and $P = 20$, respectively. This configuration results in a total of 500 β_{mnp} coefficients (41), and 5 α_m coefficients in (40).

The experimental setup is depicted in Fig. 2(a). One end of the probe is connected to a vector network analyzer (VNA) (model R140B from Copper Mountain) while the aperture is submerged in four different MUT, one at a time, i.e., methanol, acetone, 1-Propanol, dimethyl sulfoxide (DMSO), all of which have well-known permittivity [36]. The calibration procedure outlined in [3] is used in this study, with water, ethanol, and air serving as calibration materials. The measurement is done at room temperature (25°C).

Note that measurements are subject to uncertainties related to the parameters of the probe (geometric parameters and permittivity) , as well as measurement variables (frequency and temperature), all of which contribute to measurement error [34]. To minimize these variations, we used the average of 100 measurements, ensuring more accurate and consistent results. Additionally, we used standard and reference materials with a purity of 99% to improve precision.

The reflection coefficient is measured through the VNA between 1 GHz and 10 GHz at intervals of 20 MHz, resulting

$$A = \begin{bmatrix} \sum(-jk_s)^p\beta_{00p} + \frac{\epsilon_c}{\epsilon_s\gamma_0}\alpha_0 & \sum(-jk_s)^p\beta_{01p} & \cdots & \sum(-jk_s)^p\beta_{0Np} \\ \sum(-jk_s)^p\beta_{10p} & \sum(-jk_s)^p\beta_{11p} + \frac{\epsilon_c}{\epsilon_s\gamma_1}\alpha_1 & \cdots & \sum(-jk_s)^p\beta_{1Np} \\ \vdots & \vdots & \ddots & \vdots \\ \sum(-jk_s)^p\beta_{N0p} & \sum(-jk_s)^p\beta_{N1p} & \cdots & \sum(-jk_s)^p\beta_{NNp} + \frac{\epsilon_c}{\epsilon_s\gamma_N}\alpha_N \end{bmatrix} \tag{17}$$

$$B = \begin{bmatrix} \frac{\epsilon_c}{\epsilon_s\gamma_0}\alpha_0 - \sum(-jk_s)^p\beta_{00p} & -\sum(-jk_s)^p\beta_{10p} & \cdots & -\sum(-jk_s)^p\beta_{N0p} \end{bmatrix}^T \tag{18}$$

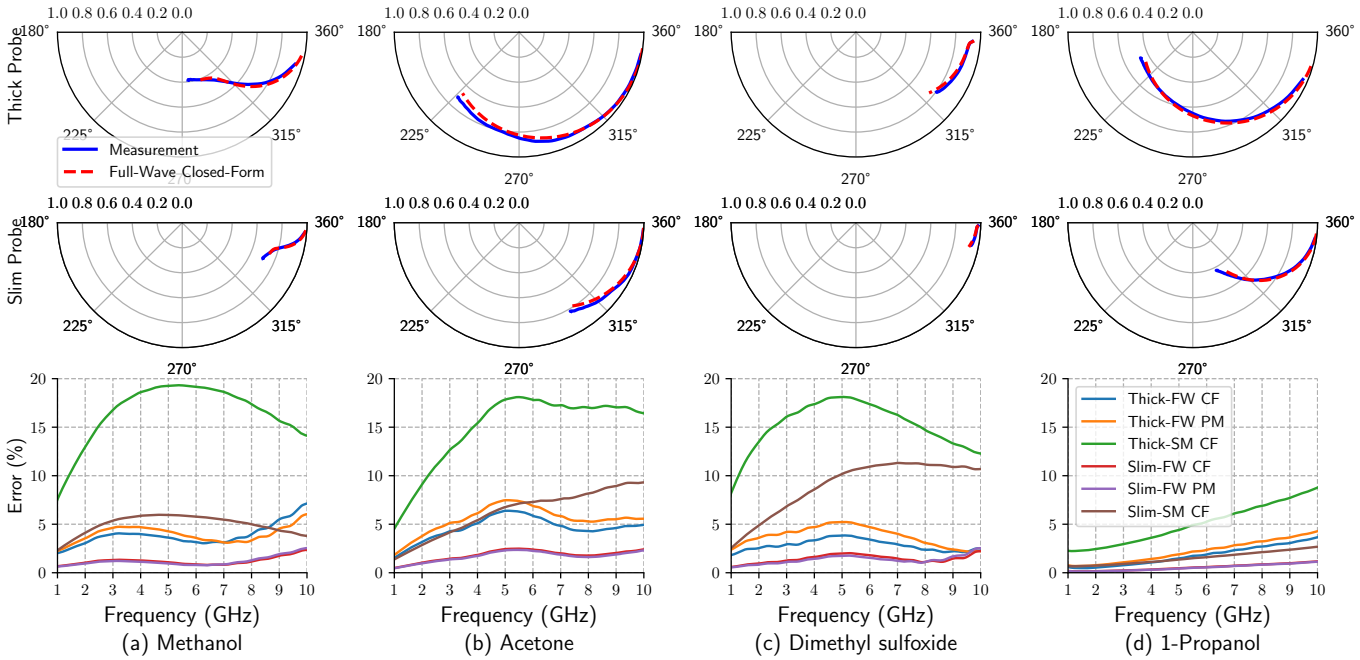

Fig. 3. Estimated reflection coefficient using the proposed model *versus* the measured reflection coefficient for (a) methanol, (b) acetone, (c) dimethyl sulfoxide (DMSO), and (d) 1-propanol over the frequency range of 1 GHz to 10 GHz. The first and second row show the results for the thick and slim probes, respectively. The third row shows the relative modelling error for the proposed full-wave closed-form model (FM-CF), along with the errors observed with the single-mode closed-form model (SM-CF) and the full-wave point-matching model (FW-PM).

in a total of 451 points for each MUT, and compared against the model predictions. All models presented earlier were implemented in Python (version 3.11) on a system with an Intel Core i7 CPU and 16 GB RAM.

The measured and model-estimated reflection coefficients for both probes and all four MUT are shown in the polar plots in Fig. 3. The first and second row correspond to the thick and slim probes, respectively. The third row shows the relative error between the measured and estimated reflection coefficient magnitude for the proposed full-wave closed-form model (FW CF), the single-mode closed-form (SM CF), and the full-wave point-matching (FW PM) models for both probes. Each column corresponds to a different MUT. The proposed model is in good agreement with the experimental results, with an error below 7%. In contrast, the single-mode closed-form model (SM CF) has a significantly higher error, reaching nearly 20% for the thick probe. The full-wave point-matching model (FW PM) and the proposed full-wave closed-form model (FW CF) show statically similar errors.

The average relative error and the processing time for each model are summarized in the top half of Table I. The processing time refers to the total duration required for the model to estimate the reflection coefficient of a material across 451 frequency points. The single-mode model shows the highest maximum average error, reaching 17.17% for the thick probe, while its performance is somewhat better for the slim probe, with a maximum error of 11.2%. It has the lowest average processing time of all models, not exceeding 2.69 seconds.

As expected, the full-wave point-matching model achieves better accuracy than the single mode model, with a maximum average error of 6.09% and 2.8% for the thick and slim probes, respectively. However, the increased accuracy comes at a cost of increased processing time, with a maximum of 144.3 seconds for the thick probe and 66.45 for the slim probe.

The proposed full-wave closed-form model maintains a similar level of accuracy to the point-matching model, with a maximum average error of 6.36% and 2.85% for the thick

TABLE I
COMPARISON OF AVERAGE RELATIVE MODELLING ERROR AND ELAPSED TIME FOR EACH MODEL - EXPERIMENTAL AND SIMULATED RESULTS

	Model	Parameter	Thick Probe				Slim Probe			
			Methanol	Acetone	DMSO	Propanol	Methanol	Acetone	DMSO	Propanol
Experimental	Single-Mode Closed-Form	Error (%)	14.1	14.0	17.2	6.68	4.04	8.59	11.2	2.03
		Time (s)	2.41	2.31	2.31	2.38	2.51	2.37	2.69	2.47
	Full-Wave Point-Matching	Error (%)	6.09	5.07	3.58	3.14	2.10	2.80	2.71	0.81
		Time (s)	132	144	141	139	32.5	57.1	65.1	66.4
	Proposed model	Error (%)	6.36	4.52	3.23	2.64	2.11	2.85	2.66	0.84
		Time (s)	2.65	2.58	2.52	2.54	3.00	2.69	2.64	2.58
	Model	Parameter	Thick Probe				Slim Probe			
			1 GHz	5 GHz	10 GHz	15 GHz	1 GHz	5 GHz	10 GHz	15 GHz
Simulation	Single-Mode Closed-Form	Error (%)	7.02	9.15	9.72	7.98	2.09	8.73	9.31	9.65
		Time (s)	2.71	2.43	2.30	2.19	2.16	4.64	2.18	2.07
	Full-Wave Point-Matching	Error (%)	2.49	2.80	0.71	3.14	1.54	4.25	4.19	2.54
		Time (s)	248	265	181	174	58.8	121	152	101
	Proposed model	Error (%)	3.54	3.95	1.18	2.25	1.43	3.86	3.78	2.18
		Time (s)	2.36	3.98	2.25	2.27	2.16	2.25	5.18	2.27

and slim probes, respectively. Yet, it does so with a processing time much closer to that of the single-mode closed-form model, with a maximum of 3.00 seconds, demonstrating a significant reduction in computational demand. This indicates that the proposed model not only improves efficiency but also maintains a level of accuracy comparable to the point-matching model, while significantly outperforming the single-mode closed-form model, especially for the thick probe.

A. Simulation Validation

To further validate the model across a wider range of MUT properties, simulations were conducted using Ansys HFSS. Fig. 2 (b) shows the simulation environment, where the blue cube represents the MUT. The MUT is symmetric cube measuring 2 cm of each side, which is significantly larger than the penetration depth of the probes. The MUT boundary condition was set to "radiation", preventing reflections from the boundaries that could interfere with the results. To improve the accuracy of the simulation, mesh refinement was performed to reach a convergence threshold of 0.01, which represents the allowable difference in S-parameters between successive mesh iterations. To validate the numerical Ansys HFSS model, simulation results where the 4 mentioned reference materials were used as the MUT were compared against the results obtained from the most accurate analytical model, i.e., the full-wave orthogonal model. An average error of less than 0.76 was observed across all materials over the frequency range of 1 GHz to 15 GHz, with increments of 20 MHz.

The real part of the relative permittivity of the MUT was swept from $\epsilon' = 1$ to $\epsilon' = 100$, and the imaginary part was swept from $\epsilon'' = 0$ to $\epsilon'' = 100$, both with increments of 5. This process was repeated at 1 GHz, 5 GHz, 10 GHz, and 15 GHz for both the thick and slim probes.

The model-estimated reflection coefficient for the the proposed model, the single-mode closed-form model, and the full-wave point-matching model are shown in polar plots of Fig. 4 for both probes. Each point on a plot corresponds to a calculated reflection coefficient for a particular model and for a unique combination of MUT complex permittivity, spanning the range provided earlier. Each column corresponds to a different frequency. The colour bar on the left indicates the relative error between the model and the simulation. As expected, the highest error, of around 20%, arises from the single-mode model. The proposed model and the full-wave point-matching model show similar errors, with a maximum of approximately 6%. The single-mode model shows its highest error when the reflection coefficient is close to zero, and the error significantly increases with frequency, highlighting the importance of considering higher-order modes. This phenomenon is also visible in the experimental results but much less pronounced in the two full-wave models.

The average relative error between each model and the simulation results, along with their computational time for a sweep of 441 material points at a single frequency, are further summarized in the bottom half of Table I. The single-mode model has the highest average error (9.72% with the thick probe at 10 GHz) and a peak error of 20%. In contrast, the proposed model and the full-wave point-matching model show similar accuracy across all simulated scenarios. Notably, the proposed model outperforms the point-matching model at 15 GHz, where it achieves a lower error for both probes. This is due to the fact that at higher frequencies the integrals in the point-matching model become more intensive to solve, increasing the level of approximation in the numerical calculations. Despite this, the proposed model maintains its accuracy while significantly reducing the processing time, with a maximum of 5.18 seconds, making it about 50 times faster than the point-matching model. These results underscore the advantage of the proposed model, offering the same level of precision as the point-matching model while dramatically reducing computational demand.

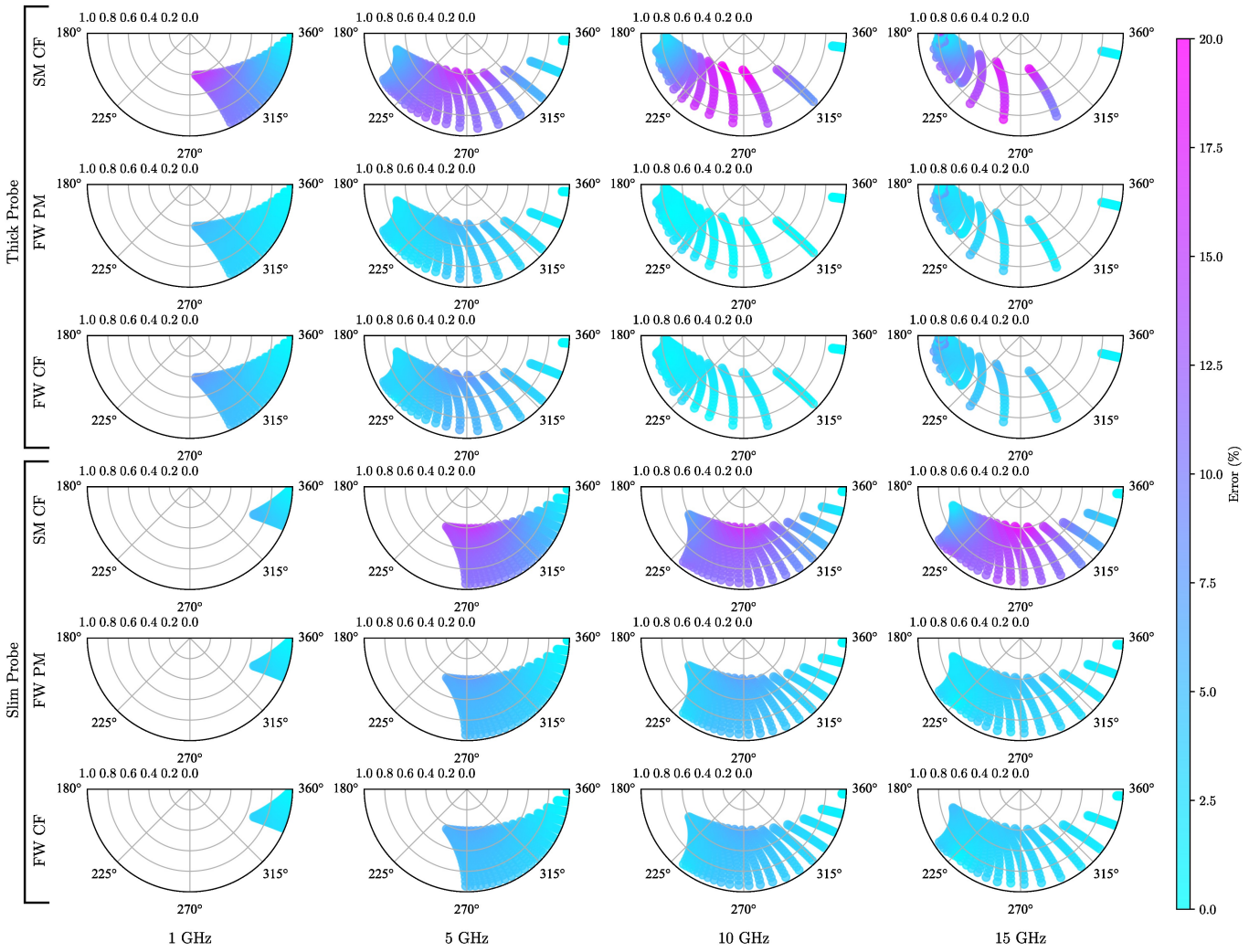

Fig. 4. Simulation results polar plots. Each point on the plot represents a combination of relative permittivity, with the real part varying from $\epsilon' = 1$ to $\epsilon' = 100$ and the imaginary part varying from $\epsilon'' = 0$ to $\epsilon'' = 100$ in increments of 5. The colour of each point indicates the error between the simulated and model-predicted reflection coefficient. Each column corresponds to a different frequency (1 GHz, 5 GHz, 10 GHz, or 15 GHz). The top three panels correspond the thick probe and the bottom 3 panel to the slim probe. Each row corresponds to a specific model, i.e., the single-mode closed-form model (CM CF), the full-wave point-matching model (FW PM), and the proposed full-wave closed-form model (FW CF).

B. Inverse Problem Validation

In the previous subsection, the model was used to calculate the reflection coefficient for a given complex permittivity of the MUT. To further validate it, we apply the model to an inverse problem, where the objective is to extract the MUT permittivity from the measured reflection coefficient. To this end we used the same MUT as in the previous experiments, for all of which the frequency dependent permittivity is well-documented. For solving the inverse problem, we follow the procedure explained in [35], [37] and use the Newton-Raphson algorithm to iteratively extract the permittivity of the MUT from the estimated reflection coefficient. From our past work in [35], 10 iterations are sufficient.

The first and second row of Fig. 5 show the real and the imaginary component of the permittivity calculated using the proposed model for each MUT as a function of frequency (solid line). These results are compared against the corresponding Debye model (dashed line) [36]. The third row shows the error between the magnitude of the model-estimated permittivity and the Debye ground truth. The left column displays the results for the thick probe, while the right column shows the results for the slim probe.

The same inverse problem was applied to the single-mode and full-wave point-matching models. The model estimation error and processing time for all models are summarized in Table II. The patterns observed in the earlier experimental and simulation results are also visible here, but with some notable differences. Specifically, the single-mode model has a significantly higher average error of 20.02%. In contrast, the proposed model achieved a maximum average error of 7%, while the full-wave point-matching model reaches 8.28%.

While our proposed model and the point-matching model show similar accuracy, a substantial difference can again be seen in the processing time. The proposed model required

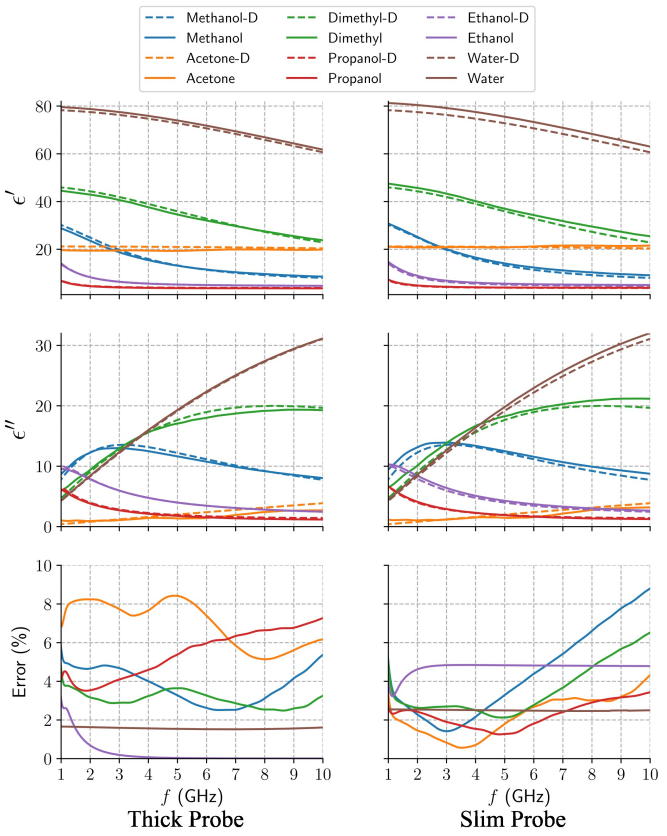

Fig. 5. Model-estimated *versus* reference permittivity of methanol, acetone, dimethyl sulfoxide (DMSO), 1-propanol, ethanol, and water. The permittivity is extracted from the measured reflection coefficient using thick and slim probes with the inverse problem approach. The first and second row display the real and imaginary parts of the measured permittivity (solid lines), respectively. The Debye model (D) is shown with dashed lines for comparison. The third row is error between the estimated permittivity using the proposed model and the Debye ground truth. The error for ethanol and water shows a smooth or constant trend over frequency, as they are the calibration materials in the measurement.

only 14.21 seconds at most per frequency sweep for each material, whereas the point-matching model took up to 5,335 seconds (approximately 1 hour and 19 minutes) to perform the same calculation. In other words, the proposed model is approximately 376 times faster than the full-wave point-matching model in solving inverse problems while delivering similar or even better accuracy in some instances. Additionally, as the proposed model employs a matrix-based method, well-developed techniques for vectorized calculations can be utilized to further reduce this processing time to just a few seconds. This drastic reduction in processing time is crucial, particularly since most applications in permittivity spectroscopy involve an inverse problem that computes permittivity across a frequency band. The ability of the proposed model to achieve faster processing times without compromising accuracy makes it highly beneficial in demanding scenarios for practical, near-to-real-time applications where computational resources and time constraints are critical.

V. Conclusion

This paper introduces a novel full-wave closed-form model for the reflection coefficient of an open-ended coaxial probe, representing a significant advancement over existing modelling approaches. Traditional models often struggle with a trade-off between accuracy and computational efficiency. Some focus exclusively on primary modes, neglecting higher-order effects and thereby compromising accuracy. Meanwhile, full-wave models generally involve complex and lengthy numerical integral calculations for each measurement, a process made even more cumbersome by singularities.

The proposed model addresses these issues effectively. By reformulating the forward model as a simple matrix inversion, where the matrix coefficients are independent of the MUT properties, we eliminate the need for repetitive numerical integration. This approach not only maintains the accuracy of full-wave models but also enables efficient vectorized calculations, which is particularly advantageous for solving the inverse problem and extract the MUT permittivity from the reflection coefficient. The model's computational speed is notably faster, with the proposed model being approximately 50 times faster in direct problems and 376 times faster in inverse problems than traditional full-wave point-matching models, while retaining comparable accuracy. This efficiency is crucial in real-time applications, such as biomedical spectroscopy, where quick and precise data acquisition is essential.

In summary, the presented full-wave closed-form model harmonizes accuracy with exceptional efficiency, overcoming the limitations of previous methods. Its capability to deliver both precise and rapid results makes it a valuable tool for applications requiring near to real-time data acquisition. A potential improvement to the proposed model is to quantify the impact of measurement uncertainty in the estimated reflection coefficient and permittivity of the MUT. These uncertainties include variations in the probe's diameter, inaccuracies in the VNA, and the dielectric properties of the reference liquids.

References

[1] K. Grenier, D. Dubuc, T. Chen, F. Artis, T. Chretiennot, M. Poupot, and J.-J. Fournie, "Recent advances in microwave-based dielectric spectroscopy at the cellular level for cancer investigations," *IEEE Trans. Microw. Theory Techn.*, vol. 61, no. 5, pp. 2023–2030, 2013.

[2] R. E. Ghiri, A. P. Saghati, E. Kaya, and K. Entesari, "A miniaturized contactless uwb microwave system for time-domain dielectric spectroscopy," *IEEE Trans. Microw. Theory Techn.*, vol. 65, no. 12, pp. 5334–5344, Dec. 2017.

[3] H. Asilian Bidgoli, N. Schieda, and C. Rossa, "On the sensitivity of bevelled and conical coaxial needle probes for dielectric spectroscopy," *IEEE Trans. Instrum. Meas.*, 2023.

[4] E. Kaya, A. P. Saghati, and K. Entesari, "A 3–10-ghz cmos time-domain complex dielectric spectroscopy system using a contactless sensor," *IEEE Trans. Microw. Theory Techn.*, vol. 67, no. 12, pp. 5202–5217, Dec. 2019.

[5] M. Elkholy and K. Entesari, "A wideband low-power lc-dco-based complex dielectric spectroscopy system in 0.18-μm cmos," *IEEE Trans. Microw. Theory Techn.*, vol. 65, no. 11, pp. 4461–4474, Nov. 2017.

[6] S. O. Nelson, "Dielectric spectroscopy in agriculture," *J. Non-Cryst. Solids*, vol. 351, no. 33-36, pp. 2940–2944, 2005.

[7] N. Wagner, M. Schwing, and A. Scheuermann, "Numerical 3-d fem and experimental analysis of the open-ended coaxial line technique for microwave dielectric spectroscopy on soil," *IEEE Trans. Geosci. Remote Sens.*, vol. 52, no. 2, pp. 880–893, Feb. 2014.

[8] K. L. Chung and S. Kharkovsky, "Monitoring of microwave properties of early-age concrete and mortar specimens," *IEEE Trans. Instrum. Meas.*, vol. 64, no. 5, pp. 1196–1203, May 2015.

TABLE II
MODEL AVERAGE RELATIVE ERROR AND ELAPSE TIME COMPARISON IN INVERSE PROBLEM

Model	Parameter	Thick Probe				Slim Probe			
		Methanol	Acetone	DMSO	Propanol	Methanol	Acetone	DMSO	Propanol
Single-Mode Closed-Form	Error (%)	14.9	20.0	15.6	14.6	8.12	12.2	9.46	8.44
	Time (s)	9.20	9.33	9.22	9.72	8.45	8.61	9.93	13.01
Full-Wave Point-Matching	Error (%)	4.29	8.28	4.12	6.83	3.77	4.22	2.84	4.26
	Time (s)	4885	5335	4913	4773	1743	2089	2078	1328
Proposed model	Error (%)	3.78	7.00	3.07	5.45	4.53	3.31	4.26	3.38
	Time (s)	13.5	13.4	14.2	14.2	13.3	14.0	13.2	11.5

[9] M. S. Ferhat, T. Honorio, T. Bore, F. Benboudjema, F. Daout, and E. Vourc'h, "Monitoring of mortar hydration combining microwave and calorimetry measurements," *IEEE Trans. Instrum. Meas.*, vol. 72, pp. 1–11, 2023.

[10] I. Ermolina, Y. Polevaya, Y. Feldman, B.-Z. Ginzburg, and M. Schlesinger, "Study of normal and malignant white blood cells by time domain dielectric spectroscopy," *IEEE Trans. Dielectr. Electr. Insul.*, vol. 8, no. 2, pp. 253–261, 2001.

[11] A. Martellosio, M. Pasian, M. Bozzi, L. Perregrini, A. Mazzanti, F. Svelto, P. E. Summers, G. Renne, L. Preda, and M. Bellomi, "Dielectric properties characterization from 0.5 to 50 ghz of breast cancer tissues," *IEEE Trans. Microw. Theory Techn.*, vol. 65, no. 3, pp. 998–1011, March 2017.

[12] S. A. R. Naqvi, A. T. Mobashsher, B. Mohammed, D. Foong, and A. Abbosh, "Benign and malignant skin lesions: Dielectric characterization, modelling and analysis in frequency band 1 to 14 ghz," *IEEE Trans. Biomed. Eng.*, 2022.

[13] C. Gabriel, S. Gabriel, and Y. Corthout, "The dielectric properties of biological tissues: I. literature survey," *Phys. Med. Biol.*, vol. 41, no. 11, p. 2231, 1996.

[14] S. Gabriel, R. Lau, and C. Gabriel, "The dielectric properties of biological tissues: Ii. measurements in the frequency range 10 hz to 20 ghz," *Phys. Med. Biol.*, vol. 41, no. 11, p. 2251, 1996.

[15] ——, "The dielectric properties of biological tissues: Iii. parametric models for the dielectric spectrum of tissues," *Phys. Med. Biol.*, vol. 41, no. 11, p. 2271, 1996.

[16] H. M. Fahmy, A. M. Hamad, F. A.-z. Sayed, Y. S. Abdelaziz, E. S. Abu Serea, A. B. E.-D. Mustafa, M. A. Mohammed, and A. M. Saadeldin, "Dielectric spectroscopy signature for cancer diagnosis: A review," *Microw. Opt. Technol. Lett.*, vol. 62, no. 12, pp. 3739–3753, 2020.

[17] M. Ambrico, M. Lasalvia, T. Ligonzo, P. Ambrico, G. Perna, and V. Capozzi, "Recognition of healthy and cancerous breast cells: Sensing the differences by dielectric spectroscopy," *Med. Phys.*, vol. 47, no. 10, pp. 5373–5382, 2020.

[18] H. A. Bidgoli, N. Schieda, and C. Rossa, "Penetration depth quantification of open-ended coaxial probes for dielectric spectroscopy of layered media," in *Proc. 2023 IEEE Can. Conf. Electron. Comp. Eng.* IEEE, 2023, pp. 94–98.

[19] B. J. Mohammed, M. Manoufali, S. A. R. Naqvi, K. S. Bialkowski, P. C. Mills, and A. M. Abbosh, "Using dielectric properties of solid fraction and water content to characterize tissues at different health and age conditions," *IEEE J. Electromagn. RF Microw. Med. Biol.*, vol. 4, no. 1, pp. 69–77, 2019.

[20] P. Mehta, K. Chand, D. Narayanswamy, D. G. Beetner, R. Zoughi, and W. V. Stoecker, "Microwave reflectometry as a novel diagnostic tool for detection of skin cancers," *IEEE Trans. Instrum. Meas.*, vol. 55, no. 4, pp. 1309–1316, Aug. 2006.

[21] M. Mertens, M. Chavoshi, O. Peytral-Rieu, K. Grenier, and D. Schreurs, "Dielectric spectroscopy: Revealing the true colors of biological matter," *IEEE Microw. Mag.*, vol. 24, no. 4, pp. 49–62, 2023.

[22] Y. Xu, F. Ghannouchi, and R. Bosisio, "Theoretical and experimental study of measurement of microwave permittivity using open ended elliptical coaxial probes," *IEEE Trans. Microw. Theory Techn.*, vol. 40, no. 1, pp. 143–150, Jan. 1992.

[23] H. Levine and C. H. Papas, "Theory of the circular diffraction antenna," *J. Appl. Phys.*, vol. 22, no. 1, pp. 29–43, 1951.

[24] N. Marcuvitz, *Waveguide Handbook*. New York: McGraw-Hill, 1951.

[25] D. K. Misra, "A quasi-static analysis of open-ended coaxial lines (short paper)," *IEEE Trans. Microw. Theory Techn.*, vol. 35, no. 10, pp. 925–928, Oct. 1987.

[26] J. Mosig, J.-C. Besson, M. Gex-Fabry, and F. E. Gardiol, "Reflection of an open-ended coaxial line and application to nondestructive measurement of materials," *IEEE Trans. Instrum. Meas.*, vol. IM-30, no. 1, pp. 46–51, March 1981.

[27] C.-L. Li and K.-M. Chen, "Determination of electromagnetic properties of materials using flanged open-ended coaxial probe-full-wave analysis," *IEEE Trans. Instrum. Meas.*, vol. 44, no. 1, pp. 19–27, Feb. 1995.

[28] H. A. Bidgoli, N. Schieda, and C. Rossa, "A closed-form full-wave model for the reflection coefficient of an open-ended coaxial probe for real-time dielectric spectroscopy," in *2024 IEEE Sensors Applications Symposium (SAS)*. IEEE, 2024, pp. 1–6.

[29] J. Galejs, *Antennas in Inhomogeneous Media: International Series of Monographs in Electromagnetic Waves*. Elsevier, 2013, vol. 15.

[30] D. M. Pozar, *Microwave engineering*. John Wiley & Sons, 2011.

[31] P. De Langhe, L. Martens, and D. De Zutter, "Measurement of low-permittivity materials based on a spectral-domain analysis for the open-ended coaxial probe," *IEEE Trans. Instrum. Meas.*, vol. 42, no. 5, pp. 879–886, Oct. 1993.

[32] S. Stuchly, C. Sibbald, and J. Anderson, "A new aperture admittance model for open-ended waveguides," *IEEE Trans. Microw. Theory Techn.*, vol. 42, no. 2, pp. 192–198, 1994.

[33] D. V. Blackham and R. D. Pollard, "An improved technique for permittivity measurements using a coaxial probe," *IEEE Trans. Instrum. Meas.*, vol. 46, no. 5, pp. 1093–1099, Oct. 1997.

[34] J. Baker-Jarvis, M. D. Janezic, P. D. Domich, and R. G. Geyer, "Analysis of an open-ended coaxial probe with lift-off for nondestructive testing," *IEEE Trans. Instrum. Meas.*, vol. 43, no. 5, pp. 711–718, Oct. 1994.

[35] H. A. Bidgoli, N. Schieda, and C. Rossa, "A simplified formulation of the reflection coefficient of an open-ended coaxial probe in multilayered media," *IEEE Trans. Microw. Theory Techn.*, 2024.

[36] A. P. Gregory and R. Clarke, "Tables of the complex permittivity of dielectric reference liquids at frequencies up to 5 ghz." 2012.

[37] J. Grant and et al., "A critical study of the open-ended coaxial line sensor technique for rf and microwave complex permittivity measurements," *J. Phys. E: Sci. Instrum.*, vol. 22, no. 9, p. 757, 1989.